Microfluidics and Nanofluidics (2024) 28:60
https://doi.org/10.1007/s10404-024-02751-x

RESEARCH

Synergistic thermal and hydrodynamic effects in 3D-printed heat sinks with intricate microchannel patterns

Win-Jet Luo[1] · Pramod Vishwakarma[2] · Bivas Panigrahi[1]

Received: 5 December 2023 / Accepted: 17 July 2024 / Published online: 5 August 2024

Abstract
A compelling solution to the issue of high heat flux generated by flexible electronic devices has been found in liquid-based microfluidic cooling devices. It has been earlier realized that the varying microchannel hydrodynamics influences the overall heat transfer in these devices. However, microfluidic cooling devices that incorporate intricate microchannels have not been explored to their full potential. In this study, we investigate the use of 3-D intricate microchannel geometries in microfluidic heat sinks, their generated hydrodynamics, and their profound impact on the overall heat transfer process. Utilizing 3D-printed scaffold removal technology, three distinct microfluidic devices were fabricated, each distinguishable by its cross-sectional shape of the microchannel designs (coil, square, and triangle). These microfluidic devices, based on Polydimethylsiloxane-Graphene oxide (PDMS-GO) as substrate material, have been examined experimentally and numerically for their heat dissipation capacities under constant temperature heat source of 358 K at flow rates ranging from 40 to 400 μL/min. Experimental observation illustrates that the coil-microchannel configuration exhibited superior heat dissipation capabilities, outperforming both the square and triangle microchannels across all flow settings. Furthermore, numerical simulations corroborated this experimental finding by providing insights into through-plane temperature distribution, heat transfer coefficient, pressure drop, and channel hydrodynamics. Our study intends to advance the understanding of microchannel cooling, as well as emphasizes the importance of geometrical configuration towards optimal electronic hotspot cooling.

Keywords Microfluidics · Intricate 3D microchannel · Heat transfer · Micro-vortices · Computational fluid dynamics (CFD)

1 Introduction

Modern electronic chips, biochips (Li et al. 2017) and micro-devices present a formidable thermal management challenge as they continue to shrink in size, become flexible by nature and are now equipped with superlative computing capabilities (Abdal-Kadhim and Leong 2018; Zhang et al. 2021). As the chips are stacked, they produce more heat per unit-area, resulting in problems such as overheating, thermal expansion, reduced performance, and even permanent chip failure (Sun and Huang 2021). In terms of heat flux, device and operational conditions determine the magnitude of heat flux density, ranging from less than 1 to over 30 kW/m^2 (Abdal-Kadhim and Leong 2018). Various thermal management strategies, including air and liquid-based heat sink technologies, have been developed in the past to keep chip operating temperatures within a safe range. Compared to traditional air-cooled heat sinks, liquid-based heat sinks have emerged as particularly advantageous due to their superior thermal properties, including higher thermal conductivity, greater density, greater stability etc. (Alihosseini et al. 2021; Varnava 2020; Zhang et al. 2015). In the last decades, a significant amount of attention has been paid towards development of liquid-based heat sinks, since they are capable of storing and transferring heat efficiently within the contact area of electronic chips, with microfluidic-based heat sinks standing out as a particularly promising approach (Maia et al. 2020; Siddiqui and Zubair 2017; Sreehari and Sharma 2019; Tullius et al.2011; Varnava 2020; Yi et al.

✉ Bivas Panigrahi
bivas@ncut.edu.tw

1 Department of Refrigeration, Air Conditioning, and Energy Engineering, National Chin-Yi University of Technology, LA403-1, Innovation R&D Building, No. 57, Sec. 2, Zhongshan Road, Taiping Dist., Taichung 41170, Taiwan

2 Graduate Institute of Precision Manufacturing, National Chin-Yi University of Technology, Taichung 41170, Taiwan

2014, 2012). Microfluidic heat sink devices are capable of enhancing cooling performance of electronic devices by precisely controlling small-scale fluid flows.

Numerous studies have built upon Qu and Mudawar's pioneering work in 2003, which explored heat transfer and pressure drop within rectangular cross-section microchannels (Qu and Mudawar 2002). To comprehensively understand heat transfer characteristics across various flow regimes, numerous experimental and numerical investigations have been conducted, both with single channels and multiple channels arranged in parallel (Asadi et al. 2014; Gharaibeh et al. 2022; Ghobadi and Muzychka 2015; Omosehin et al. 2022; Roy et al. 2013; Luo 2009). One common observation that emerged from these studies was the absence of fluid mixing for commonly employed straight microchannels. In the absence of mixing, boundary layers developed along the microchannel walls, ultimately hindering heat transfer from the chips to the surface. Microfluidic heatsinks with serpentine channels, pin–fin structures, ribs, were developed to address this issue (Gholami et al. 2018; Sreehari and Sharma 2019; Zhang et al. 2021). These channels introduce secondary flows (Luo et al. 2004) and chaotic advection, which inherently disrupt boundary layers, thus promoting heat transfer without a substantial increase in pumping power (Sreehari and Sharma 2019). Nevertheless, recent researches have revealed some interesting aspects of these unique channel designs, which may create small yet stagnant vortices in these channels and may create localized hot spots in the heat sinks affecting the overall performance of the device (Renfer et al. 2013; Sreehari and Sharma 2019). For instance, in the study (Sreehari and Sharma 2019), the authors have demonstrated that sharp bends in 2-D microchannels could result in fluid stagnation regions, negatively affecting the overall thermal performance of microfluidic heatsinks. Over the period, it has been further realized that the heatsinks with 2-D channel designs often do not facilitate efficient through-plane heat transfer within the devices.

3D-printed microfluidic heat sinks is considered as a promising solution for electronic hotspot cooling because they provide greater control over design parameters, enabling intricate geometries to be created, which in turn optimize fluid–solid contact within the device for maximum heat transfer (Gharaibeh et al. 2022; Luo et al. 2022, 2023; Maia et al. 2020; Marschewski et al. 2017; Nafis et al. 2021). In addition, microfluidic devices fabricated utilizing 3-D printing scaffold removal technologies can be tailored with PDMS-nanocomposite as the heat sink material with improved thermal conductivity characteristics, ensuring optimal heat transfer rates for specific applications (Luo et al. 2022, 2023; Yi et al. 2014). 3D printing also creates enhanced surface roughness, which can enhance the nucleate boiling process, resulting in efficient phase-change heating (Bian et al. 2018). Gharaibeh et al. (2022) proposed 3D-printed liquid cooled heat sink further equipped with guide vanes for multi-core hotspot cooling. Compared to existing devices, it has a thermal resistance benchmark of 0.036 °C/W and chip non-uniformity index of 0.81 °C, which is significantly higher than its counterparts.

The silicone elastomer PDMS (polydimethylsiloxane) is an ideal choice for making microfluidic heat sinks since it has several benefits such as chemical stability and mechanical flexibility upon curing, even at extreme temperatures (Amerian et al. 2019; Chan et al. 2015). Despite its benefits, PDMS has a relatively low thermal conductivity of approximately 0.07 W/m–K. This limitation adversely affects the heat transfer efficiency of heat sink devices (Yi et al. 2014). In order to alleviate this previously mentioned problem, nano-fillers such as alumina oxides, carbon nanotubes, metallic fillers, and graphene nanoparticles have been dispersed into PDMS in order to enhance its overall thermal properties (Aramesh et al. 2019; Chałupniak and Merkoçi 2017; Luo et al. 2022, 2023; Wang et al. 2022; Wei et al. 2020; Yi et al. 2014). Nevertheless, thermal performance of PDMS-based composite as the host material of microfluidic heat sinks has only been investigated in a limited number of research reports (Luo et al. 2022, 2023; Yi et al.2014). Studies have shown that PDMS-GO nanocomposite materials, which consist of 5% *w/w* GO nanoparticles, can be utilized for the fabrication of microfluidic heat-sinks for mitigating the heat load of high-flux electronics equipment (Chałupniak and Merkoçi 2017; Luo et al. 2022, 2023). GO sheets are highly conductive, which makes them ideal for thermal management in modern electronics. By incorporation of 5% *w/w* (GO) into polydimethylsiloxane (PDMS) has been observed to enhance the thermal conductivity, elasticity, and root mean square roughness value of PDMS by a margin of 2.5-fold, threefold, and 8.7-fold, respectively (Luo et al. 2022). These microfluidic heat sink devices have also demonstrated exceptional mechanical flexibility, making them suitable for flexible heatsink applications.

In spite of earlier research showing that channel hydrodynamics (Luo et al. 2023; Renfer et al. 2013; Sreehari and Sharma 2019) can influence heat transfer, microfluidic heat sink device hydrodynamics embedded with intricate microchannels have not yet been fully explored. Thus, the objective of this study is to investigate the 3-D intricate microchannel geometries as the flow carrying mediums in microfluidic heat sinks and their profound impact on overall heat transfer. We leverage the innovative 3D-printed scaffold removal techniques (Maia et al. 2020; Saggiomo and Velders 2015) to create microfluidic heat sink devices with different shapes of microchannels; specifically coil, square, and triangle type cross-section geometry. These microfluidic devices use PDMS-GO as substrate material, for an improved thermal propagation from the hot-spot material to the environment. The performance of these devices has been experimentally observed at various operating conditions. The numerical analyses were further conducted and validated with experimental results to evaluate the effectiveness of various heatsink devices.

2 Materials and methods

Figure 1A–D schematically illustrates three distinct microfluidic heat-sink devices, each distinguished by their cross-sectional shape of microchannels (coil, square, and triangle). To avoid nomenclature confusion, we have referred to the coil-like channel device as Device I, the square-like channel device as Device II, and the triangular-like channel device as Device III. The fabrication of microfluidic heat sink devices (Fig. 1E) was carried out using the technology of removing 3D-printed scaffolds (Maia et al. 2020). The fabrication of a microchannel scaffold was accomplished employing a 3D printer (E2. Raise 3D Technologies Inc., CA, USA) and acrylonitrile butadiene styrene (ABS) material. The printer's resolution was as finer as 0.2 mm on the Z-axis and 0.4 mm on the XY-axis. The microchannel scaffold was subsequently attached with the pillars with the 3D-printed Polylactic acid (PLA) based mold using a solder-iron. The mold used for fabricating the PDMS-GO device had dimensions of 50 mm in length, 30 mm in width, and 6 mm in height, which are precisely the final dimensions of the PDMS-GO microfluidic heat sink device itself. The host material for preparing the heat-sink device was fabricated using composition of PDMS-GO material. To prepare the nanocomposite base material, 5% *w/w* of the GO nanopowder (P-ML20, Energae Inc.) was uniformly dispersed into PDMS (Sylgard184, Dow corning) through shear mixing employing mechanical stirrer (LC-OES-200SH) rotating at 200 rpm for a period of 15 min. The mean particle size, average thickness and specific surface area of the graphene oxide (GO) utilized in

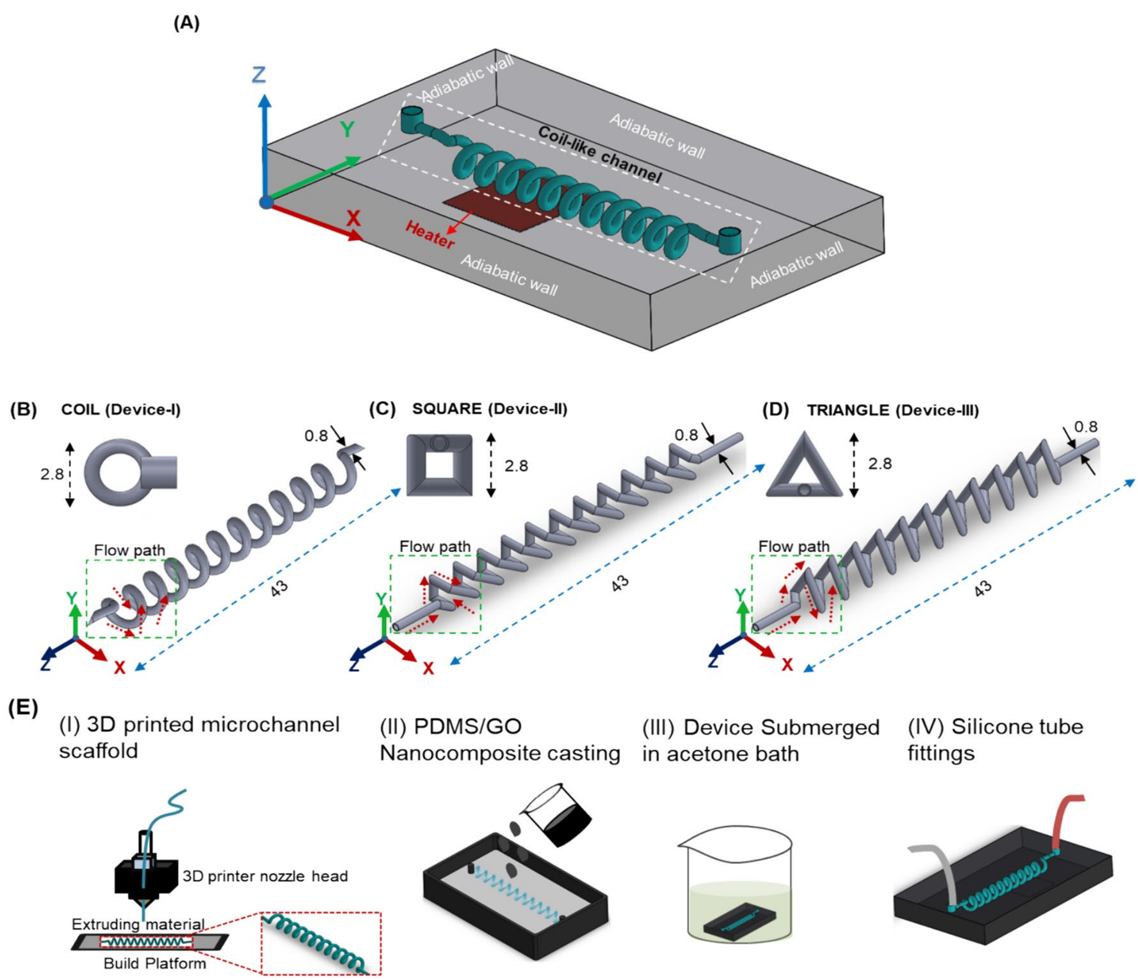

Fig. 1 Schematic depiction of the design and fabrication of microfluidic device. **A** Geometry and dimension of different heat sink devices distinguished by the cross-sectional shape of microchannels i.e. **B** coil, **C** square, and **D** triangle channel. **E** Schematic demonstration of step-by-step procedure of heat-sink device fabrication. All dimensions are in mm

the study were 10.60 ± 3.6 μm, 5 nm, 25 ± 5 m^2/g, respectively. Nanocomposite mixtures were degassed for 30 min in a vacuuming device (Rocker 300, Taiwan) before casting to eliminate any confined air-bubbles. The composite material of PDMS-GO was then introduced into the microfluidic device mold and baked over a hot-plate maintained at constant temperature of 40 °C for 24 h. The resulting device was subsequently immersed in an acetone bath and sonicated up to 6 h to remove the scaffold channel to form the anticipated microchannel cavities within the heat sink device. Furthermore, to investigate the effect of prolonged exposure of acetone on the hydraulic diameter of the microchannel cavity, a stereomicroscope (SV-5, Sage Vision, Taiwan) in conjunction with an industrial digital camera (E3ISPM, TOUPCAM, ToupTek Photonics Co. Ltd, China) was employed. The average hydraulic diameter was measured at 873.54 ± 56.06 μm, in comparison to the 3-D printed mold's diameter of 800 μm. This indicates a minimal discrepancy of approximately 9.2% between the intended and the actual hydraulic diameter (ESI figure s1). The hydraulic diameter of the channel falls within the range of 1–1000 μm, fitting comfortably within the parameters to be described as the microfluidic devices (Nielsen et al. 2019; Rosa et al. 2009). For the additional testing, silicone tubing was integrated to the inlet-port and outlet-port, and microfluidic devices were firmly attached within an additively manufactured device holder.

Figure 2 illustrates the experimental platform. For the experimentation, 3D-printed device holders were used to hold the microfluidic heat-sinks. Microchannel holders have a squared cavity that holds ceramic heaters with dimensions of 10 mm × 10 mm × 1.2 mm (W × L × H). To adjust the temperature of the ceramic heater, a direct current power source (DCPS) (GPE-2323, GW Instek, Taiwan) was used. Since most electronic hotspots are around 358 K (Abdal-Kadhim and Leong 2018), in our case, a DC power supply was used to keep the ceramic heater's temperature constant throughout the experiment at 358 K with a power supply of 3.7 V and 0.14 A. DI water was used as the flow medium and introduced into the microfluidic heat-sink using a syringe pump (KDS 230, Kd scientific). All experiments were performed at the room temperature of (~298 K). Thermal management efficacies of microfluidic heatsink devices were investigated for various flow rates of 40, 120, 240, and 400 μL/min. The resolution and the detector pitch (pixel size) of the infrared (IR) camera (FLIR, A-315, Teledyne Inc. Ontario, Canada) employed in the study were designated as 320 × 240 pixels and 25 μm respectively, as per the company datasheet. The spectral

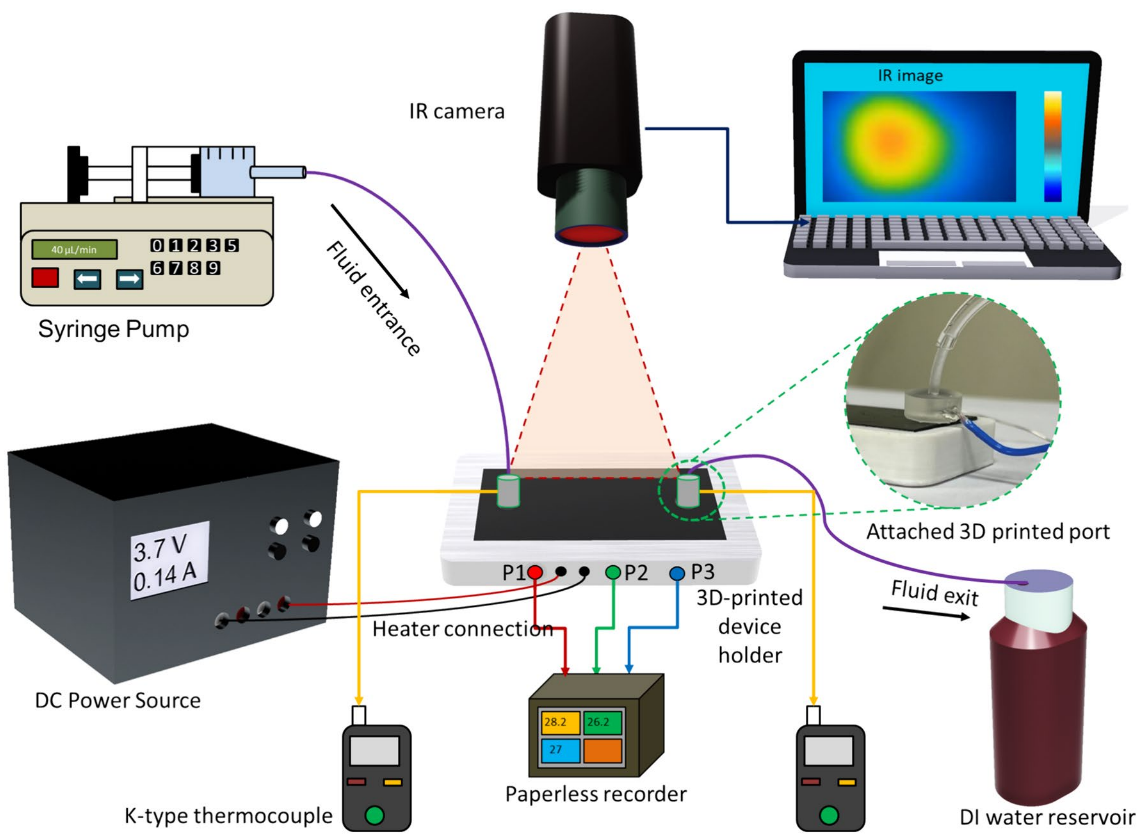

Fig. 2 Experimental test-rig for thermal characterization of microfluidic heat sinks

range of the camera was in the range of 7.5–13 µm. For the study, the acquisition frequency of IR camera was set at 60 Hz. The detailed specifications of the IR camera are illustrated in the ESI supplementary table s1. The initial measurement of the average hotspot temperature was recorded at the 0th minute, coinciding with the activation of the syringe pump to regulate fluid flow and the engagement of the DC power source to energize the ceramic heater, both operations initiated simultaneously. After the initial measurement, the hotspot temperature was meticulously recorded with an IR camera at 5-min intervals for up to 20 min, by which time the device had reached steady-state conditions. The IR images of the heatsink devices were captured at 20 min, when the devices had already achieved steady state.

The experimental data were analyzed using commercial tool by FLIR software (Teledyne Inc., Ontario, Canada). On the top surface of the microchannel device, we have identified the hotspot at the center of the ceramic heater, located ~14 mm away from the fluid entrance, and recorded time-lapse temperature data. In addition, K-type thermocouples (TES-1319A, TES Corp., Taiwan) were installed at the inlet and outlet to record the temperature variation of fluid. To install the thermocouples, a device was fabricated using stereolithography (SLA) 3D printer (Form 3, Formlabs, Somerville, USA), as demonstrated in the inset picture of Fig. 2. To further assess the base temperatures of the heatsink devices (T_{p1}, T_{p2}, T_{p3}), K-type thermocouples were affixed at three distinct locations along the length of the base of the microfluidic heatsink device and data were recorded through paperless data recorder (PR20, Brain child, Taiwan). The IR camera settings remained consistent throughout the experiment.

The Eq. 1 below calculates the total heat input (Q), when DC power is applied to the ceramic heater by adjusting voltage (V) and current (I).

$$Q = VI \tag{1}$$

The overall heat flux (q) was based on the total base area ($A_b = \mathrm{L} \times \mathrm{W} = 50 \times 30\ \mathrm{mm}^2$) of the microfluidic heat sink device and is given by the underneath Eq. 2.

$$q = \frac{Q}{A_b} \tag{2}$$

The Reynold number (Re) in our study depends on the hydraulic diameter of the microchannel as illustrated by the underneath Eq. 3.

$$\mathrm{Re} = \frac{\rho_f U D_h}{\mu} \tag{3}$$

where ρ_f is the density of water, U is the inlet velocity, D_h is the hydraulic diameter of the microchannel and μ is the dynamic viscosity. In addition, the inlet velocity is directly proportional to the imposed flow rate V, given by Eq. 4.

$$V = U \cdot A_c \tag{4}$$

where, A_c is the cross-sectional area of the microchannel.

Global heat transfer coefficient (h) quantified in the study can be given by the following Eq. 5 (Sreehari and Sharma 2019).

$$h = \frac{q}{\Delta T_m} \tag{5}$$

where, ΔT_m is the mean temperature difference between the average temperature of the bottom wall of the microchannel (3 individual points p1, p2 and p3) and the average temperature between fluid inlet and outlet. The heat transfer coefficient was estimated using the mean temperature difference ($\Delta \mathrm{T}_m$) between the average temperature of the bottom wall and the temperature difference in the fluid (Sreehari and Sharma 2019; Wu and Cheng 2003; Wang and Ding 2008; Xu et al. 2005).

$$\Delta T_m = \left(T_{p1} + T_{p2} + T_{p3}\right)/3 - \left(T_{f,in} + T_{f,out}\right)/2 \tag{6}$$

where, T_{p1}, T_{p2}, T_{p3} are the onset temperature of three individual points p1, p2 and p3 of bottom wall of the heat sink (ESI Fig. 3). $T_{f,in}$ and $T_{f,out}$ are the temperature of the working fluid (water) at inlet and outlet. Temperature difference (ΔT) between the flow inlet and outlet through the microchannel, calculated using an Eq. 7.

$$\Delta \mathrm{T} = T_{f,out} - T_{f,in} \tag{7}$$

IR imaging experimental procedures do not explicitly explain the through-plane temperature propagation capability of any microfluidic heat sink. To shed light on the through-plane temperature distribution, heat transfer coefficient, pressure-drop and the hydrodynamics generated within the microfluidic channel, three-dimensional (3D) numerical models were employed. In this aspect, 3D design of the device was developed utilizing a commercially available CAD software, namely Solidworks. A tetrahedral type of mesh was generated throughout the domain, where the upper limit for skewness recorded to be as high as 0.82, whereas the lower limit of orthogonality was as low as 0.152, which authorizes excellent quality of mesh since both the parameters satisfied its acceptable limit <0.95 and >0.1 respectively (Fatchurrohman and Chia 2017). Considering that there is a continuous heat transfer between the solid and fluid, a conjugate heat transfer model was employed using commercially available CFD software ANSYS fluent solver. Four different flow conditions were simulated: 40, 120, 240, and 400 µL/min, in order to assess the thermal performance of the devices. Considering the hydraulic diameter of 0.08 mm, laminar flow regimes were identified as Re-numbers ranging from 1.06 to 10.6. Considering steady state, all the related physical equations (mass, momentum and energy) were solved. As listed below, certain assumptions were made to develop the numerical model;

a. The flow within the microchannel was considered to be continuous and laminar.
b. The nature of fluid was incompressible and single phase.
c. Steady-state heat transfer was considered.
d. Effect of thermal radiation was neglected.
e. No slip at solid–fluid interface.
f. Physical properties of the fluid and solid remain unchanged throughout the study.

Considering the above assumption, the Navier–Stokes (N–S) equations, consisting of the continuity equation, energy equation and momentum equation (eqns. 8–10) were solved for the fluid domain (water).

Continuity equation in the fluid zone $\nabla \cdot \mathbf{U} = 0$ (8)

Momentum equation for the fluid $\rho_f(\mathrm{U} \cdot \nabla)\mathbf{U} = -\nabla \mathrm{P} + \mu \nabla^2 \mathbf{U}$ (9)

Energy equation in the fluid domain $\rho_f c_{p,f}(\mathbf{U} \cdot \nabla \mathrm{T}_f) = k_f \nabla^2 \mathrm{T}_f$ (10)

In the case of a solid domain (PDMS-GO), only the energy equation needs to be addressed because the velocity (U) is zero in this domain.

Energy equation(solid domain) $\nabla \cdot (k_s \nabla \mathrm{T}_s) = 0$ (11)

where ρ, **U**, P, μ, T, k, and c_p are the density, velocity vector, pressure, dynamic viscosity, temperature, thermal conductivity, and heat capacity. Whereas, suffix *f* and *s* denotes the fluid and solid domain respectively. Inlet fluid flow conditions were varied according to the flow conditions, and constant pressure outlets were selected for the outlet. Working fluid was selected as water-liquid from the Fluent database and fluid inlet temperature was 298 K (ambient condition), while material properties (e.g. thermal conductivity, specific heat, and density) were determined from experimental results (Luo et al. 2022) and listed in ESI Table 2. At the bottom of the device, a uniform heat flux of 2158 W/m^2 was applied to the ceramic heater, while all other walls, except for the top surface, were considered adiabatic. The equation ($q'' = VI/A_s$) was used to set the desired heat flux at the heater surface, where q'', V, I, and A_s represent the heat flux at the heater surface, voltage, current, and overall surface area of the heater, respectively. The calculation was initialized using the hybrid scheme, while a second order up-wind algorithm was implemented to discretize the momentum and energy equations. A coupled scheme was selected for the coupling process of pressure–velocity, and the least square cell method was applied for spatial discretization of the gradients. The residuals were set as the order of 10^{-6}, which generally demonstrates the tightly convergence criterion. The free convection heat transfer coefficient of air was assumed to be 10 W/m^2 K due to the heat sink device's exposed top surface (Yi et al. 2014). To quantitatively measure the magnitude of rotational flow dynamics within microfluidic channels, vorticity (ω was utilized, which is mathematically defined by the curl of the velocity field (Panigrahi et al. 2018).

$$\omega = \nabla \times \mathbf{U} \tag{12}$$

where, U is the velocity vector field.

The CFD models were verified and validated using the grid independence test (refer to ESI Fig. 2) and comparing the results with experimental results (Fig. 3), respectively. The correlation coefficients (*r*-value) between the experimental outcomes and CFD for Device I (coil), Device II (square), and Device III (triangle) were estimated to be 0.97, 0.95, and 0.97, respectively, indicating a high degree of correlation and a consistent trend with the lowest T_{max} for the coil channel for both the simulation and experimental findings. However, it was observed that the proposed CFD model tends to underestimate the T_{max} values compared to the experimental values at a lower flow rate. This discrepancy might be due to the simplified assumption of steady-state conditions in the model, as opposed to the realistic transient conditions in practical experimental cases. Additionally, the slight increase in the microchannel diameter due to acetone treatment in the experimental setup could also contribute to this difference.

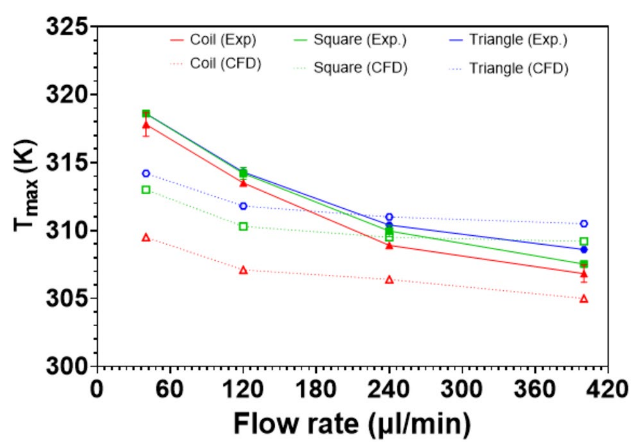

Fig. 3 Numerical simulation (CFD) results were validated with the experimentally obtained results by comparing the maximum hot spot temperature (T_{max}) along the top surface of the microfluidic heat sink devices for Device I, coil type microchannel (*r*-value >0.97), Device II, square type microchannel (*r*-value >0.94), Device III, triangle type microchannel (*r*-value >0.95)

3 Results and discussions

3.1 Experimental thermal characterization

In the proposed microfluidic heatsink device that uses intricate microchannels with DI water as working medium, heat transfer from the chip (~heat emitting surface) to the surface primarily occurs through a combination of conduction and convection mechanisms. Initially, the heat generated by the chip conducts through the PDMS-GO nanocomposite material towards the low and side-walls of the microchannels. Once it reaches these microchannels, the embedded fluid acts as a coolant, absorbing the conducted heat. As the fluid flows through the channels, convection becomes the dominant mode of heat transfer. Through passive cooling, the cold fluid removes the absorbed heat from the chip surface. The intricate design of microchannels enhances the surface area in contact with the coolant, optimizing the rate of heat removal. In the context of microchannel design, efficient design indicates sufficient heat removal. As a result, the chip temperature is effectively reduced, when it reaches to the surface of the heat sink device. A low temperature on the surface of a heatsink is a clear indicator of efficient heat transfer within the system as it suggests that the heat is being effectively spread out and dissipated into the environment rather than accumulating over the potential hotspot region. Temperature measurements at the hotspot were recorded at 5-min intervals up to the 20-min mark, by which time, the device had reached a steady state (ESI Fig. 4). The steady-state temperature distribution contours over the top surface for all the heatsink devices for different flow rates of 40, 120, 240, and 400 μL/min were quantified and illustrated through IR imaging (Fig. 3A). The hotspot appears to be located ~14 mm away from the fluid entrance for all the devices, and the magnitude of temperature tends to decrease corresponding to increase in the flow rates. Among all the cases, Device-I (coil-microchannel configuration) exhibited the lowest hotspot temperature (left column of the Fig. 3A). This observation is corroborated by the diminishing temperature distribution (as evidenced by the less intense red contours in the coil devices), which becomes increasingly less pronounced with higher flow rates, unlike in the other two devices. To further assess the effectiveness of heat transfer, two critical parameters were evaluated: the average hot-spot surface temperature of the chip (T_{avg}) and the temperature difference between the inlet ($T_{f,in}$) and outlet ($T_{f,out}$) of the working fluid (water) flowing through the microchannels, denoted as ΔT. These parameters serve as indicators of efficient heat conduction and convection, respectively.

To evaluate the change to surface temperature for all the devices (Device I-III), a region of interest (ROI) just above the hotspot, where temperature distribution is more prominent was marked (Refer to Device-I, 40 μL/min in Fig. 3A). The average steady-state temperature (T_{avg}) was calculated across the hotspot region (ROI) along the microfluidic heat sink device's length, based on three separate measurements (N = 3) (Fig. 4B). Device I displayed the lowest hotspot temperature followed by Device II and Device III for all the flow rates. For illustration, for a flow rate of 40 μL/min, the average hotspot temperature (T_{avg}) at 20 min was recorded as 315, 316 and 317 K, respectively for Device I, II and III. A similar trend was noticed for other flow rates of 120, 240 and 400 L/min. Further for Device I, the average temperature was reduced as a magnitude of ~13 K, when the flow rate was tuned from 40 to 400 μL/min, highlighting the hydrodynamic influence on overall heat transfer. A similar trend was noticed for the other devices. It can be further noted that all the intricate channels outperforms the conventional straight circular channels (ESI Fig. 5). To further validate the aforementioned trend, the difference of inlet and outlet temperatures ($\Delta T = T_{f,in} - T_{f,out}$) of the working fluid (water) flowing through the microchannel were calculated for various flow rates (Fig. 4B). From the experimental observation, Device I has a larger value of fluid temperature difference compared to Device II and Device III, concurrent to our earlier observation highlighting the effectiveness of heat removal by Device I. A substantial difference in temperature change (ΔT) was observed for a flow rate of 240 μL/min in Device-I, with a ΔT approximately 3 and 2 K higher than that measured in Device-II and Device-III, respectively. Further observations revealed that for Device I, as the flow rate increased from 240 to 400 μL/min, the temperature difference (ΔT) decreased from 8.7 to 7.2 K. This trend was consistent across both devices and could be attributed to a decrease in fluid interaction time (heat transfer time). This behavior may be related to the hydrodynamics within the microchannel, and was further explored through detailed numerical simulations in subsequent sections.

3.2 Numerical estimation of through-plane temperature distribution

One of the major limitations of IR thermography is that it cannot provide information on through-plane heat transfer. Therefore, systematic 3D numerical calculations were performed under different operating conditions to estimate the temperature distribution along the thickness of the developed microfluidic heatsink devices. For further analysis, Plane-1 was selected, which is located 17 mm from the substrate's upper end (Fig. 5A). All analyses were conducted at a constant temperature of 358 K. For an understanding of the physics underlying the unique heat transfer for each devices at various flow conditions, we extracted

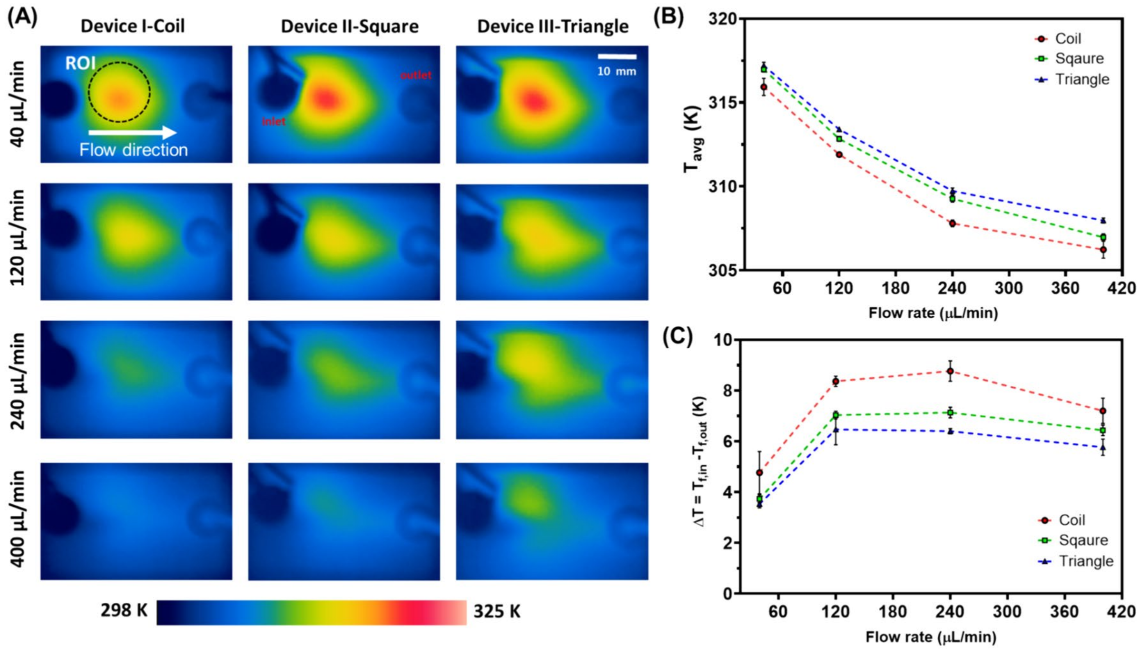

Fig. 4 Thermal characterization of tested microfluidic heatsink devices for various flow rates of 40, 120, 240, and 400 μL/min. **A** Temperature contours of tested heatsink devices under different flow conditions. **B** Average hot-spot temperature (T_{avg}) across ROI for all flow rates. **C** Temperature difference (ΔT) between flow inlet ($T_{f,in}$) and flow outlet ($T_{f,out}$). The results are represented in Mean ± SEM (N = 3)

the temperature profiles along the line A–A' and displayed them non-dimensionally (Fig. 5B–E). It was observed that among the tested 3D microchannels designs, the coil channel exhibited the most favorable temperature distribution along the line A–A'. As observed, the surface temperature of Device I was accounted to be at least onefold lower than Device III for the flow rate of 40 μL/min^{-1} (Fig. 4B). When the flow rates were increased from 40 to 400 μL/min, a significant decrease in temperature magnitude was observed across all devices. The coil microchannel, however, showed the most substantial temperature drop. For instance, as flow rate was tuned at 400 μL/min, the surface temperature of the Device I is roughly two-fold better than that of the Device III (Fig. 5E). This emphasizes the hydrodynamic influence on overall heat transfer and confirms the experimental trend observed earlier.

3.3 Heat transfer characteristics

The heat transfer coefficient (*h*) as a function of the Reynolds number (*Re*) was quantified from both experimental and numerical observations for all tested devices (Fig. 6A). It was observed that for all the intricate channels, *h* tends to increase corresponding to the increase in *Re*. In both data sets, Device I demonstrated the highest magnitude of *h* among the three tested devices for all flow rates. From the experimental observations, the average heat transfer coefficient for Device I was quantified as 91.8 W/m^2-K, which is 1.58 times and 1.92 higher than that of Device II (57.85 W/m^2-K) and Device III (47.65 W/m^2-K). Numerical quantifications closely matched the experimental estimations, with Device I having the highest *h*-value, followed by Device II and Device III. The correlation coefficients (*r*-value) between the experimental outcomes and CFD for Device I, Device II, and Device III were estimated to be 0.80, 0.80, and 0.89, respectively, indicating a high degree of correlation and a consistent trend. However, it was observed that the proposed CFD model tends to underestimate the *h* values compared to the experimental values. This discrepancy arises due to the nature of the calculation procedure: in the experiment, the average surface temperature was quantified from three individual points (refer to ESI Fig. 3), whereas in the CFD analysis, it was quantified from the area-weighted average of the whole surface, which is comparatively lower. Considering the heat transfer coefficient is a measure of the fluid's convection capability and is used to describe the rate at which heat is transferred from the heatsink surface to the fluid flowing through the microchannels, higher *h* values for Device I indicate a higher cooling efficiency and can allow designing of smaller heat sinks. Subsequently, the pressure drop of the fluid ($\Delta P = P_{in} - P_{out}$) was quantified from the numerical simulations. The pressure drop was found to be optimal for Device I, followed by Device II, Device III, and the straight circular microchannel.

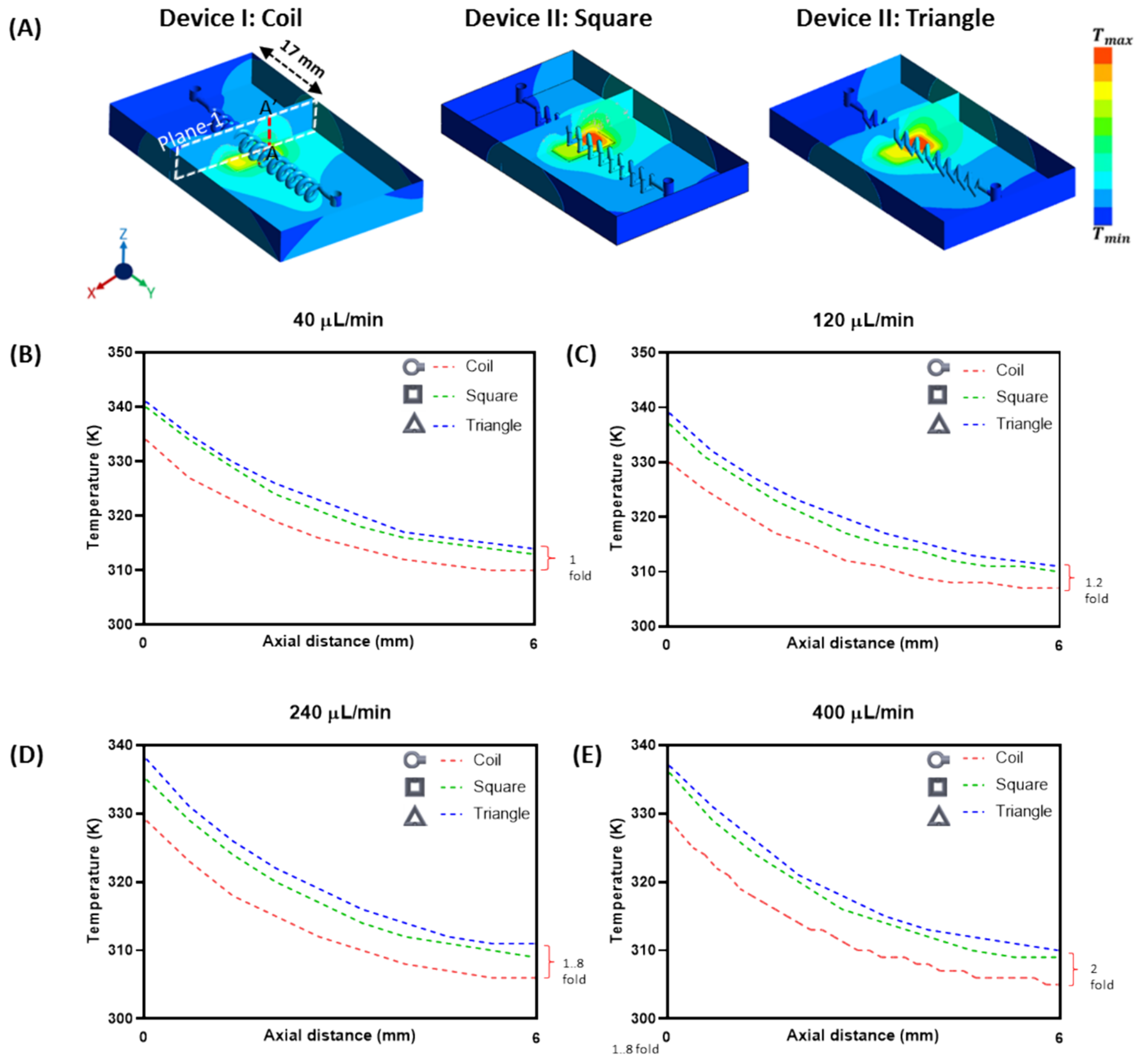

Fig. 5 Through-plane temperature distribution for tested microfluidic heatsink devices. **A** Temperature contours for devices. Through-plane temperature extracted along line A–A' (6 mm) for corresponding flow rates of **B** 40, **C** 120, **D** 240, and **E** 400 µL/min, respectively

Among all the tested devices, Device I exhibited the maximum pressure drop for all flow rates (Fig. 6B). For instance, for a flow rate of 400 µL/min, for Device I, ΔP was computed to be 243.52 Pa, whereas for Device II and Device III, it was estimated to be 164.02 and 143.25 Pa, respectively. Conversely, the straight circular microchannel of the same hydraulic diameter displayed the lowest pressure drop compared to the 3D microchannel devices, regardless of the *Re*. This trend aligns with previous observations that optimized microchannel structures tend to experience increased pressure drops, thereby requiring increased pumping power (Zhu et al. 2022; Lori and Vafai 2022).

The proposed 3D microchannel demonstrated higher pressure drops with increasing Reynolds numbers (*Re*). Therefore, it is important to evaluate thermohydraulic enhancement factor (TEF, η) to assess the effectiveness of these microchannels despite the increased pressure drop penalties. TEF is defined as the ratio of heat transfer enhancement to the pressure drop penalty between the intricate structures (i.e., coil, square, and triangle) and the baseline structure (straight circular channel). The expression for TEF can be given as follows: (Webb 1981; Zhao et al. 2016; Bhandari and Prajapati 2021).

$$TEF(\eta) = \frac{Nu/Nu_o}{(\Delta p/\Delta p_o)^{1/3}} \tag{13}$$

where, Nu, and Δp are the Nusselt number and pressure drop for the devices with intricate microchannel with improved heat transfer. Whereas, Nu_o and Δp_o are the Nusselt number and pressure drop for the microfluidic device with straight circular microchannel structure. Figure 6C demonstrates the variation of the TEF as a function of the *Re*. Considering that it serves as a baseline for comparison, the TEF value for

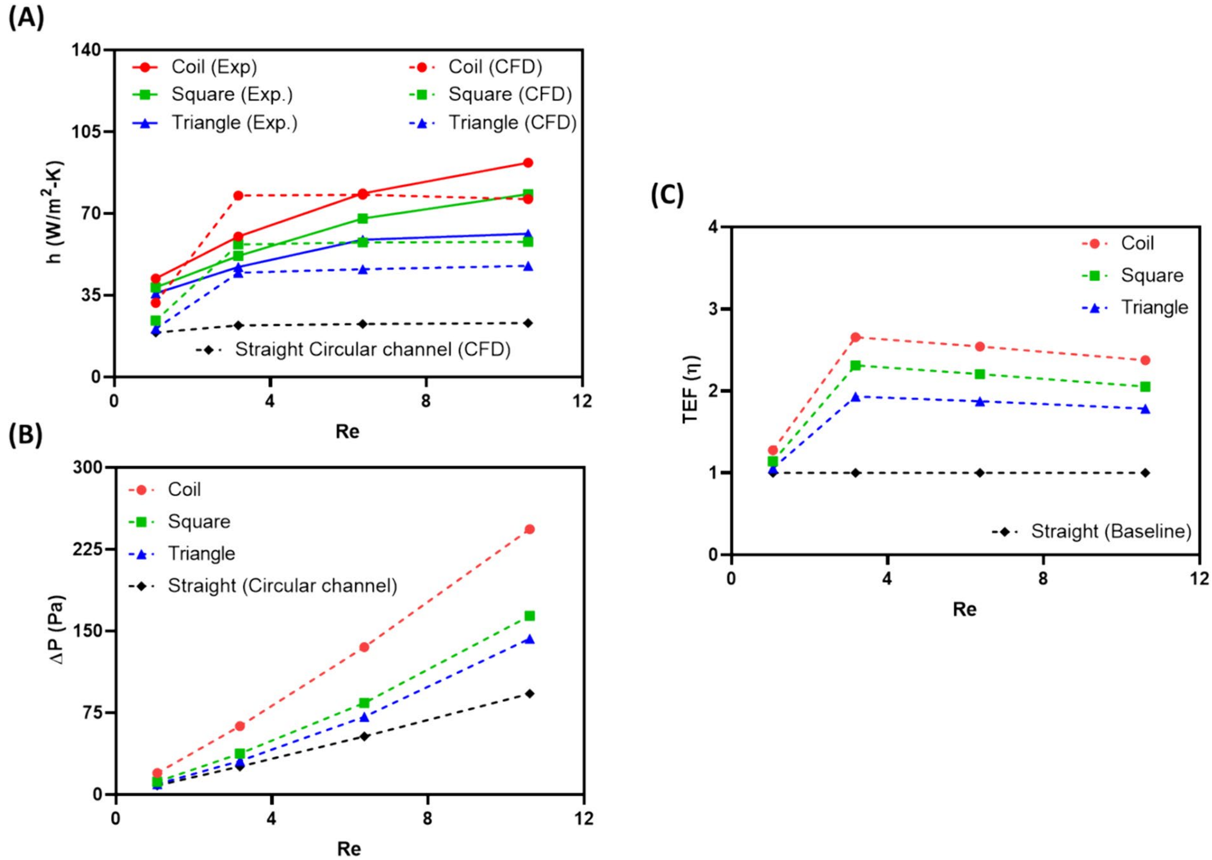

Fig. 6 Heat transfer characteristics of various devices as a function of Reynolds number. **A** Heat transfer coefficient, *h* (Experiment and CFD), and **B** pressure drop, Δ*P* (CFD) and **C** thermohydraluic enhancement factor, TEF (CFD)

the conventional straight microchannel is considered unity regardless of *Re*. As observed, the TEF values for the Device I, Device II, and Device III are consistently greater than unity across various Reynolds numbers, indicating superior performance of intricate channels. A similar trend is noticed for all 3D microchannel devices, with TEF values increasing significantly when *Re* reaches 3.18. After this steep rise, there is a slight drop in TEF; however, it remains above 1.5 for all 3D microchannels across all *Re*. This indicates that the enhancement in heat transfer is sufficient to offset the increased pumping power. Among the devices, the heat sink with a coil-like 3D microchannel (Device I) is preferred due to its superior *h* as well as TEF value, especially for all *Re*. However, it is not yet clear why the coil channel outperforms its counterparts. It is very likely that the hydrodynamics within these intricate channels of the heat sink devices have a significant impact on their heat transfer characteristics. To clarify this further, a detailed hydrodynamic analysis is conducted and presented in the next section of the manuscript.

3.4 Hydrodynamic study of intricate channel designs on the thermal efficacy

A detailed numerical analysis was carried out for various operating conditions to determine the hydrodynamic impact of various microchannel designs on overall heat transfer. For flow visualization, a cross-sectional area referred as Plane-A is selected at a distance of 15 mm from the left side of the microfluidic heat sink. The flow was visualized using a cross-sectional plane indicated by the black dotted circle in the central region (Fig. 7A). The velocity magnitude contours superimposed with velocity streamlines are depicted for all the operating conditions to visualize any existing vortices corresponding to increase in flow *Re* (Fig. 7B–D). Based on the curl of the velocity vector field (Δ × U), we quantified the vorticity (ω) for different devices. There were no vortices observed for Device-I, even at a relatively higher flow rates of 400 μLmin^{-1} (Fig. 7B). For Device II, with square microchannel, two distinct micro vortices were being

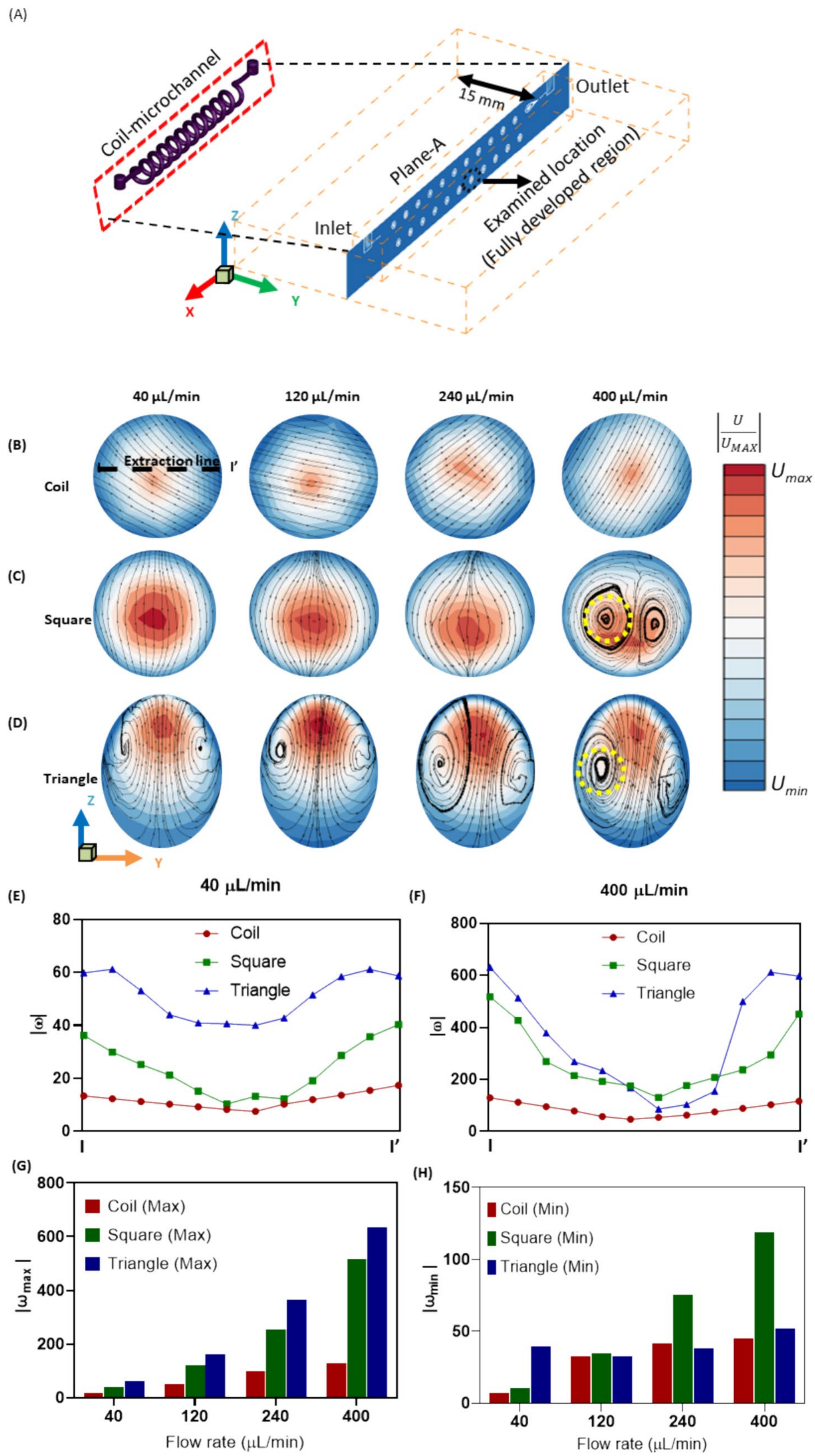

Fig. 7 Hydrodynamic analysis of different 3D microchannels for different flow conditions. **A** A schematic depiction of the device with the selected plane for vorticity analysis. Vorticity contours are superimposed with velocity streamlines at different flow rates for **B** Device I with coil type microchannel, **C** Device II with square-microchannel and **D** Device III with triangle-microchannel. The yellow dotted circles were adopted for the quantification of circulation Γ. The magnitude of the vorticity extracted along line I–I' at axial distance of Z = 0.4 mm **E** for minimum flow rate of 40 μL/min, **F** and maximum flow rate of 400 μL/min. For all the tested flow rates **G** The maximum vorticity, $|\omega_{max}|$ and **H** The minimum vorticity, $|\omega_{min}|$

noticed near the microchannel wall at higher flow rate of 400 μL/min (Fig. 7C). These two vortices are observed to be more distinguished in the case of Device III with triangular microchannel, even for a flow rate of 120 μL/min (Fig. 7D). A similar observation was also made for two-dimensional (2-D) microchannel, where sharp bends formed micro-vortices in the vicinity of micro channel walls (Sreehari and Sharma 2019). The magnitude of the vortices produced was measured along an axial line designated as I–I' at z = 0.4 mm. Regardless of the microchannel designs, the magnitude of vortices was observed to be directly proportional to the magnitude of the flow rate. Furthermore, Device I has the lowest magnitude of vorticity, while Device III has the highest magnitude (Fig. 7E–H). For instance, at a flow rate of 40 $\mu Lmin^{-1}$, the peak magnitude of the vortices $|\omega_{max}|$ was estimated as 17, 40 and 61 s^{-1} for coil, square and triangle-microchannel respectively, which increased to 130, 518 and 634 s^{-1}, corresponding to the increase to the flow rate of 400 $\mu Lmin^{-1}$ (Fig. 7E–F). It was further observed that, in Device I, the peak magnitude of the vorticity ($|\omega_{max}|$) at a flow rate of 400 μL/min nearly matches the minimum magnitude of the vortices ($|\omega_{min}|$) for Device III (Fig. 7G–H). Apart from that, it was further observed that Device I implies a relatively narrow range of vortex strength ($|\omega_{max}| - |\omega_{min}|$) compared to other two devices indicating stable flow conditions and uniformity in flow, which might be beneficial for the overall heat transfer. These trends can be directly correlated to earlier experimental findings, which underscores that Device I exhibited the lowest average hotspot temperature (T_{avg}) and the maximal temperature difference between the flow inlet and flow outlet (ΔT) compared to its counterparts. Considering that the circulation magnitude ($\Gamma(t) = \oint_c \vec{u} \cdot \vec{ds}$) is a measure of the strength of vorticity and is attributed to the driving force of fluid flow diffusion, it was calculated for all the devices (Panigrahi et al. 2018). For 400 $\mu Lmin^{-1}$, the $\Gamma(t)$ for the Device II and Device III within the vortex core (yellow circle in Fig. 7C–D), computed as 51.5 and 59.2 mm^2/s, respectively. Since the heat transfer characteristics for Device III were suboptimal and those for Device I were optimal, the magnitude of vorticity and circulation can be directly correlated to the devices' heat transfer characteristics. Apparently for Device III, micro vortices near the sharp boundary of microchannel walls contain stagnant fluid zone. These static fluid may create a boundary layer that limits the efficient heat transfer from the source to the fluid flow. Apart from that these static fluid recirculates with respect to time and create micro vortices due to the fluid shear. It can be noted that when fluid is trapped in a vortex, it creates a static area of fluid that is warmer than the surrounding fluid due to continuous heat transfer from the heater, leading to a stationary fluid hotspot. Similar phenomena were earlier highlighted in the literatures (Luo et al. 2023; Renfer et al. 2013; Sreehari and Sharma 2019), that these types of micro-vortices generate undesired localized hotspots over time and negatively impacts the overall effectiveness of heat transfer in microfluidic heat sink devices. Renfer et al. 2013 performed thorough experimental research to measure the static liquid hotspots within the microvortices area of the heatsink, which can be 4 °C warmer than the surrounding area. Sreehari and Sharma 2019 found that sharp bends in 2-D microchannels created areas where fluid stagnated, negatively impacting the thermal efficiency of microfluidic heatsinks. Due to the sharp bends in Device II and Device III, the micro-vortex regions formed at high flow rates, impacting the overall heat transfer. Considering there are no such micro-vortices observed in the Device I with coil type microchannel and with lowest average hotspot temperature (T_{avg}), highest temperature gradient from inlet to outlet (ΔT), higher heat transfer coefficient (h) and low pressure drop (ΔP), the heat dissipation of this device can be considered efficient and is recommended towards the design of microfluidic heat sink devices.

4 Conclusions

Three different microfluidic heat sink devices with distinct 3-D intricate microchannels were investigated using experimental and numerical approaches to elucidate the impact of channel designs on the overall heat transfer. An additive manufacturing technology followed by a PDMS-nanocomposite material casting was used towards the fabrication of the heat sink. The heat dissipation efficacies were assessed for different devices at different flow rate conditions for a constant hot-spot temperature of 358 K. The heatsink device with coil-microchannel presented a higher heat dissipation capacity with lower hotspot temperature followed by square and triangle microchannel for all the tested flow rates. On top of that, with higher flow rate tuning, Device I with coil-type microchannel, indicated overall high through-plane temperature, high heat transfer coefficient and a smaller pressure drop compared to its counterparts indicating an efficient heat dissipating efficacy. Further hydrodynamic analysis elucidates micro-scale vortices near the edge of square and triangle microchannel due to the sharp bending's in their geometries. These microscale vortices are more prominent at higher flow rates. The formation of micro-scale vortices augmented the localized fluid rotation around the edges of the sharp bends and indicates a possible heat entrapment and recirculation within the fluid increasing temperature of localized hotspot. Thus, it is appropriate to utilize coil-microchannels within microfluidic heat sink devices towards improved thermal management. It is expected that such innovative 3D printed microfluidic heat sinks will ensure optimal device performance while ensuring their longevity in light of the escalating demands of high-performance computing.

Supplementary Information The online version contains supplementary material available at https://doi.org/10.1007/s10404-024-02751-x.

Acknowledgements The National Science and Technology Council (NSTC) of Taiwan supported the research of Dr. Bivas Panigrahi under grant number NSTC 111-2221-E-167-016.

Author Contribution W.J.L: Resources, Software, Supervision, P.V: Data curation, Formal analysis, Investigation, Methodology, Writing-Original draft preparation, B.P: Conceptualization, Formal analysis, Funding acquisition, Investigation, Project administration, Resources, Supervision, Visualization, Writing-original draft, reviewing & editing.

Data Availability No datasets were generated or analysed during the current study.

Declarations

Conflict of interest The authors declare no competing interests.

References

Abdal-Kadhim AM, Leong KS (2018) Application of thermal energy harvesting in powering WSN node with event-priority-driven dissemination algorithm for IOT applications. J Eng Sci Technol 13:2569–2586

Alihosseini Y, Bari AR, Mohammadi M (2021) Effective parameters on increasing efficiency of microscale heat sinks and application of liquid cooling in real life. Adv Microfluid Nanofluids

Amerian M, Amerian M, Sameti M, Seyedjafari E (2019) Improvement of PDMS surface biocompatibility is limited by the duration of oxygen plasma treatment. J Biomed Mater Res A 107:2806–2813

Aramesh S, Doostmohammadi A, Rezai P (2019) Poly (dimethylsiloxane)/Cu/Ag nanocomposites: electrical, thermal, and mechanical properties. Polym Compos 40:4093–4101

Asadi M, Xie G, Sunden B (2014) A review of heat transfer and pressure drop characteristics of single and two-phase microchannels. Int J Heat Mass Transf 79:34–53

Bhandari P, Prajapati YK (2021) Thermal performance of open microchannel heat sink with variable pin fin height. Int J Therm Sci 159:106609

Bian H, Kurwitz C, Sun Z, Cheng K, Chen K (2018) Enhanced nucleate boiling on 3D-printed micro-porous structured surface. Appl Therm Eng 141:422–434

Chałupniak A, Merkoçi A (2017) Graphene oxide–poly (dimethylsiloxane)-based lab-on-a-chip platform for heavy-metals preconcentration and electrochemical detection. ACS Appl Mater Interfaces 9:44766–44775

Chan HN, Chen Y, Shu Y, Chen Y, Tian Q, Wu H (2015) Direct, one-step molding of 3D-printed structures for convenient fabrication of truly 3D PDMS microfluidic chips. Microfluid Nanofluid 19:9–18

Fatchurrohman N, Chia S (2017) Performance of hybrid nano-micro reinforced mg metal matrix composites brake calliper: simulation approach. In: IOP conference series: materials science and engineering. IOP Publishing, p 012060

Gharaibeh AR, Tradat MI, Rangarajan S, Sammakia BG, Alissa HA (2022) Multi-objective optimization of 3D printed liquid cooled heat sink with guide vanes for targeting hotspots in high heat flux electronics. Int J Heat Mass Transf 184:122287

Ghobadi M, Muzychka YS (2015) Heat transfer and pressure drop in mini channel heat sinks. Heat Transf Eng 36:902–911

Gholami MR, Akbari OA, Marzban A, Toghraie D, Shabani GAS, Zarringhalam M (2018) The effect of rib shape on the behavior of laminar flow of oil/MWCNT nanofluid in a rectangular microchannel. J Therm Anal Calorim 134:1611–1628

Li D-Y, Zhang H, Cheng J-P, Li X-B, Li F-C, Qian S, Joo SW (2017) Numerical simulation of heat transfer enhancement by elastic turbulence in a curvy channel. Microfluid Nanofluid 21:1–16

Lori MS, Vafai K (2022) Heat transfer and fluid flow analysis of microchannel heat sinks with periodic vertical porous ribs. Appl Therm Eng 205:118059

Luo WJ (2009) Effect of ionic concentration on electrokinetic instability in a cross-shaped microchannel. Microfluid Nanofluid 6(2):189–202

Luo WJ, Pan YJ, Yang RJ (2004) Transient analysis of electro-osmotic secondary flow induced by dc or ac electric field in a curved rectangular microchannel. J Micromech Microeng 15(3):463

Luo W-J, Vishwakarma P, Hsieh C-C, Panigrahi B (2022) Microfluidic modular heat sink with improved material characteristics towards thermal management of flexible electronics. Appl Therm Eng 216:119142

Luo W-J, Vishwakarma P, Panigrahi B (2023) Hydrodynamic influence on thermal management of flexible heatsink devices embedded with out-of-plane intricate microchannel design. Int Commun Heat Mass Transf 144:106792

Maia I, Rocha C, Pontes P et al (2020) Heat transfer and fluid flow investigations in PDMS microchannel heat sinks fabricated by means of a low-cost 3D printer. In: Ren Y (ed) Advances in microfluidic technologies for energy and environmental applications. IntechOpen, p 133

Marschewski J, Brenner L, Ebejer N, Ruch P, Michel B, Poulikakos D (2017) 3D-printed fluidic networks for high-power-density heat-managing miniaturized redox flow batteries. Energy Environ Sci 10:780–787

Nafis BM, Whitt R, Iradukunda A-C, Huitink D (2021) Additive manufacturing for enhancing thermal dissipation in heat sink implementation: a review. Heat Transf Eng 42:967–984

Nielsen JB, Hanson RL, Almughamsi HM et al (2019) Microfluidics: innovations in materials and their fabrication and functionalization. Anal Chem 92(1):150–168

Omosehin OS, Adelaja AO, Olakoyejo OT, Oyekeye MO (2022) Numerical study of the thermal performance and pressure drops of water-based Al_2O_3-Cu hybrid nanofluids of different compositions in a microchannel heat sink. Microfluid Nanofluid 26:49

Panigrahi B, Lu C-H, Ghayal N, Chen C-Y (2018) Sperm activation through orbital and self-axis revolutions using an artificial cilia embedded serpentine microfluidic platform. Sci Rep 8:1–9

Qu W, Mudawar I (2002) Experimental and numerical study of pressure drop and heat transfer in a single-phase micro-channel heat sink. Int J Heat Mass Transf 45:2549–2565

Renfer A, Tiwari MK, Tiwari R, Alfieri F, Brunschwiler T, Michel B, Poulikakos D (2013) Microvortex-enhanced heat transfer in 3D-integrated liquid cooling of electronic chip stacks. Int J Heat Mass Transf 65:33–43

Rosa P, Karayiannis TG, Collins MW (2009) Single-phase heat transfer in microchannels: the importance of scaling effects. Appl Therm Eng 29(17–18):3447–3468

Roy P, Anand N, Banerjee D (2013) Numerical simulation of flow and heat transfer in radially rotating microchannels. Microfluid Nanofluid 15:397–413

Saggiomo V, Velders AH (2015) Simple 3D printed scaffold-removal method for the fabrication of intricate microfluidic devices. Adv Sci 2:1500125

Siddiqui OK, Zubair SM (2017) Efficient energy utilization through proper design of microchannel heat exchanger manifolds: a comprehensive review. Renew Sustain Energy Rev 74:969–1002

Sreehari D, Sharma AK (2019) On thermal performance of serpentine silicon microchannels. Int J Therm Sci 146:106067
Sun B, Huang X (2021) Seeking advanced thermal management for stretchable electronics. Npj Flex Electron 5:1–5
Tullius JF, Vajtai R, Bayazitoglu Y (2011) A review of cooling in microchannels. Heat Transf Eng 32:527–541
Varnava C (2020) Chips cool off with integrated microfluidics. Nat Electron 3:583–583
Wang Y, Ding GF (2008) Experimental investigation of heat transfer performance for a novel microchannel heat sink. J Micromech Microeng 18(3):035021
Wang S, Feng D, Guan H et al (2022) Highly efficient thermal conductivity of polydimethylsiloxane composites via introducing "Line-Plane"-like hetero-structured fillers. Compos A Appl Sci Manuf 157:106911
Webb RL (1981) Performance evaluation criteria for use of enhanced heat transfer surfaces in heat exchanger design. Int J Heat Mass Transf 24(4):715–726
Wei J, Liao M, Ma A et al (2020) Enhanced thermal conductivity of polydimethylsiloxane composites with carbon fiber. Compos Commun 17:141–146
Wu HY, Cheng P (2003) An experimental study of convective heat transfer in silicon microchannels with different surface conditions. Int J Heat Mass Transf 46(14):2547–2556
Xu JL, Gan YH, Zhang DC, Li XH (2005) Microscale heat transfer enhancement using thermal boundary layer redeveloping concept. Int J Heat Mass Transf 48(9):1662–1674
Yi P, Kayani AA, Chrimes AF, Ghorbani K, Nahavandi S, Kalantar-zadeh K, Khoshmanesh K (2012) Thermal analysis of nanofluids in microfluidics using an infrared camera. Lab Chip 12:2520–2525
Yi P, Awang RA, Rowe WS, Kalantar-zadeh K, Khoshmanesh K (2014) PDMS nanocomposites for heat transfer enhancement in microfluidic platforms. Lab Chip 14:3419–3426
Zhang J, Zhao Y, Diao Y, Zhang Y (2015) An experimental study on fluid flow and heat transfer in a multiport minichannel flat tube with micro-fin structures. Int J Heat Mass Transf 84:511–520
Zhang Z, Wang X, Yan Y (2021) A review of the state-of-the-art in electronic cooling. e-Prime Adv Electr Eng Electron Energy 1:100009
Zhao J, Huang S, Gong L, Huang Z (2016) Numerical study and optimizing on micro square pin-fin heat sink for electronic cooling. Appl Therm Eng 93:1347–1359
Zhu Q, Su R, Xia H, Zeng J, Chen J (2022) Numerical simulation study of thermal and hydraulic characteristics of laminar flow in microchannel heat sink with water droplet cavities and different rib columns. Int J Therm Sci 172:107319